Ghostbursting: A Novel Neuronal Burst Mechanism

Brent Doiron[*], Carlo Laing[*], André Longtin[*], and Leonard Maler[#]

[*]*Physics Department, University of Ottawa, 150 Louis Pasteur, Ottawa, Ontario, Canada K1N 6N5*

[#]*Department of Cellular and Molecular Medicine, University of Ottawa, 451 Smyth Road, Ottawa, Canada K1H 8M5*

Word Count Abstract: 225
Word Count Introduction: 1013
Word Count Discussion: 1844
Number of Text Pages: 28
Number of Figures: 13
Number of Tables: 1

Corresponding author:
Brent Doiron
Physics Department
University of Ottawa
Ottawa, Ontario
Canada K1N 6N5
Phone: (613) 562-5800 (8096)
FAX: (613) 562-5434
Email: bdoiron@physics.uottawa.ca

Abstract

Pyramidal cells in the electrosensory lateral line lobe (ELL) of weakly electric fish have been observed to produce high frequency burst discharge with constant depolarizing current (Turner et al., 1994). We present a two-compartment model of an ELL pyramidal cell that produces burst discharges similar to those seen in experiments. The burst mechanism involves a slowly changing interaction between the somatic and dendritic action potentials. Burst termination occurs when the trajectory of the system is reinjected in phase space near the "ghost" of a saddle-node bifurcation of fixed points. The burst trajectory reinjection is studied using quasi-static bifurcation theory which shows a period doubling transition in the fast subsystem as the cause of burst termination. As the applied depolarization is increased, the model exhibits first resting, then tonic firing, and finally chaotic bursting behaviour, in contrast with many other burst models. The transition between tonic firing and burst firing is due to a saddle-node bifurcation of limit cycles. Analysis of this bifurcation shows that the route to chaos in these neurons is type I intermittency, and we present experimental analysis of ELL pyramidal cell burst trains which support this model prediction. By varying parameters in a way that changes the positions of both saddle-node bifurcations in parameter space we produce a wide gallery of burst patterns, which span a significant range of burst time scales.

1 – Introduction

Burst discharge of action potentials is a distinct and complex class of neuron behaviour (Connors et al., 1982; McCormick et al., 1985; Connors and Gutnick, 1990). Burst responses show a large range of time scales and temporal patterns of activity. Many electrophysiological studies of cortical neurons have identified cells that intrinsically burst at low frequencies (<20 Hz) (Bland and Colom, 1993; Steriade et al., 1993; Franceschetti et al., 1995). However, recent work in numerous systems has now identified the existence of "chattering" cells which show burst patterns in the high frequency γ range (>20 Hz) (Turner et al., 1994; Paré et al., 1995; Gray and McCormick, 1996; Steriade et al., 1998; Lemon and Turner, 2000; Brumburg et al., 2000). Also, the specific inter-spike interval (ISI) pattern within the active phase of bursting varies considerably across burst cell types. Certain bursting cells show a lengthening of ISIs as a burst evolves (e.g. pancreatic-β cells, Sherman et al., 1990), others a parabolic trend in the ISI pattern (e.g *Aplysia* R15 neuron; Adams 1985), and yet others show

response to stimuli. This may have consequences for the information content of the cell's output

(Lisman, 1997).

JCNS 811-

obtained. However, in that study we modeled the proximal apical dendrite with ten compartments, five of which contained active spiking Na$^+$ channels. The large number of variables in such a model is incompatible with the objectives of the present study. In light of this, and following previous modeling studies involving action potential backpropagation (Pinsky and Rinzel, 1994; Bressloff, 1995; Mainen and Sejnowski, 1996; Lánsky and Rodriguez, 1999; Wang, 1999; Booth and Bose, 2001), we investigate a two-compartment model of an ELL pyramidal cell, where one compartment represents the somatic region, and the second the entire proximal apical dendrite. Note that a two-compartment treatment of dendritic action potential backpropagation is a simplification of the cable equation (Keener and Sneyd, 1998). However, in consideration of the goals of the present study, which require only DAP production, the two-compartment assumption is sufficient.

2.2 Two-Compartment Model

A schematic of our two-compartment model of an ELL pyramidal cell is shown in Figure 2, together with the active inward and outward currents that determine the compartment membrane potentials. Both the soma and dendrite contain fast inward Na$^+$ currents, $I_{Na,s}$ and $I_{Na,d}$, and outward delayed rectifying (Dr) K$^+$ currents, respectively $I_{Dr,s}$ and $I_{Dr,d}$. These currents are necessary to reproduce somatic action potentials, and proper spike backpropagation that yields somatic DAPs. In addition, both the soma and dendrite contain passive leak currents I_{leak}. The membrane potentials V_s (somatic) and V_d (dendritic) are determined through a modified Hodgkin/Huxley (1952) treatment of each compartment. The coupling between the compartments is assumed to be through simple electrotonic diffusion giving currents from soma to dendrite , $I_{s/d}$, or vice-versa, $I_{d/s}$. In total, the dynamical system comprises six nonlinear differential equations, Eq (1)-(6); henceforth, we will refer to Eq(1)-(6) as the *ghostburster* model, and the justification for the name will be presented in the Results section.

Soma

(1) $\quad \dfrac{dV_s}{dt} = I_S + g_{Na,s} \cdot m_{\infty,s}{}^2(V_s) \cdot (1-n_s) \cdot (V_{Na} - V_s) + g_{Dr,s} \cdot n_s{}^2 \cdot (V_K - V_s)$

$\quad\quad\quad + \dfrac{g_c}{\boldsymbol{k}} \cdot (V_d - V_s) + g_{leak} \cdot (V_l - V_s)$

(2) $\quad \dfrac{dn_s}{dt} = \dfrac{n_{\infty,s}(V_s) - n_s}{\boldsymbol{t}_{n,s}}$

Dendrite

(3) $\quad \dfrac{dV_d}{dt} = g_{Na,d} \cdot m_{\infty,d}{}^2(V_d) \cdot h_d \cdot (V_{Na} - V_d) + g_{Dr,d} \cdot n_d{}^2 \cdot p_d \cdot (V_K - V_d)$

$\quad\quad\quad + \dfrac{g_c}{(1-\boldsymbol{k})} \cdot (V_s - V_d) + g_{leak} \cdot (V_l - V_d)$

(4) $\quad \dfrac{dh_d}{dt} = \dfrac{h_{\infty,d}(V_d) - h_d}{\boldsymbol{t}_{h,d}}$

(5) $\quad \dfrac{dn_d}{dt} = \dfrac{n_{\infty,d}(V_d) - n_d}{\boldsymbol{t}_{n,d}}$

(6) $\quad \dfrac{dp_d}{dt} = \dfrac{p_{\infty,d}(V_d) - p_d}{\boldsymbol{t}_{p,d}}$

Table I lists the values of all channel parameters used in the simulations. The soma is modeled with two variables (see eq. (1) and (2)). The reduction from the classic four dimensional Hodgkin-Huxley model is accomplished by slaving $I_{Na,s}$ activation, $m_{\infty,s}$, to V_s (i.e the Na$^+$ activation m_s tracks V_s instantaneously), and modeling its inactivation ,h_s, through $I_{Dr,s}$ activation, n_s (we set $h_s \equiv 1 - n_s$). This second approximation is a result of observing in our large compartmental model (Doiron et al., 2001b) that $h_s + n_s \approx 1$ during spiking behaviour. Both of these approximations

have been used in various other models of spiking neurons (Keener and Sneyd, 1998). The dendrite is modeled with four variables (see eq. (3)-(6)). Similar to the treatment of $I_{Na,s}$, we slave $I_{Na,d}$ activation, $m_{\infty,d}$, to V_d, but model its inactivation with a separate dynamical variable h_d. Lemon and Turner (2000) have shown that the refractory period of dendritic action potentials is larger than that of somatic in ELL pyramidal neurons. This result has previously been shown to be necessary for burst termination (Doiron et al., 2001b). To model differential somatic/dendritic refractory period we have chosen $\tau_{h,d}$ to be longer than $\tau_{n,s}$

inactivation of somatic Dr,s since somatic spikes observed in bursting ELL pyramidal cells do not exhibit broadening as the burst evolves (Lemon and Turner, 2000).

The somatic-dendritic interaction is modeled as simple electrotonic diffusion with coupling coefficient g_c, and scaled by the ratio of somatic-to-total surface area κ. This form of coupling has been used in previous two-compartment neural models (Mainen and Sejnowski, 1996; Wang 1999; Kepecs and Wang, 2000; Booth and Bose, 2001). I_S represents either an applied or synaptic current flowing into the somatic compartment. In the present study I_S is always constant in time, and will be used as a bifurcation parameter. Physiological justification for the parameter values given in Table I is presented in detail in Doiron et al. (2001b). Eqs (1) – (6) are integrated by a 4th order Runge-Kutta algorithm with a fixed time step of $\Delta t = 5 \times 10^{-6}$ s.

3 – Results

3.1 Model performance

Figure 3*A* and 3*B* show simulation time series of V_s and p_d, respectively, for the ghostburster with constant depolarization of $I_S = 9$. We see a repetitive burst train similar to that shown in Figure 1*A*. Figure 4 compares the time series of V_s and V_d for the ghostburster (bottom row) during a single burst, to both a somatic and dendritic burst from ELL pyramidal cell recordings (top row), and the large compartmental model presented in Doiron et al., (2001b) (middle row). All burst sequences are produced with constant somatic depolarization. The somatic bursts all show the same characteristic growth in depolarization (DAP growth), and consequent decreases in ISI leading to the high frequency doublet. The dendritic bursts all show that a dendritic spike failure is associated with both doublet spiking and burst termination. The somatic AHPs in the simulation of the ghostburster do not show a gradual depolarization during the burst, as do both the AHPs in the ELL pyramidal cell recordings and the large compartmental model simulations. This is a minor discrepancy, which is not relevant for the understanding of the burst

hyperpolarization of the somatic membrane, mediated by somatic potassium activation n_s, allows electrotonic diffusion of the dendritic action potential, creating a DAP in the somatic compartment. However, with repetitive spiking the dendritic action potentials, shown by V_d, broaden in width and show a baseline summation (Figure 4). This is due to the slow inactivation of $I_{Dr,d}$, mediated by p_d, as shown in Figure 3B. This further drives electrotonic diffusion of the dendritic action potential back to the soma; consequently, the DAP at the soma grows, producing an increased somatic depolarization as the burst evolves. This results in decreasing somatic ISIs, as experimentally observed during ELL burst output. This positive feedback loop between the soma and dendrite finally produces a high frequency spike doublet (Figure 4).

Doublet ISIs are within the refractory period of dendritic spikes but not that of somatic spikes (Lemon and Turner, 2000). This causes the backpropagation of the second somatic spike in the doublet to fail, due to lack of recovery of $I_{Na,d}$ from its inactivation, as shown in the dendritic recordings (Figure 4). This backpropagation failure removes any DAP at the soma, uncovering a large bAHP, and thus terminates the burst. This creates a long ISI, the inter-burst period, which allows p_d and h_d to recover, in preparation for the next burst (see Figure 3B).

3.2 Bifurcation Analysis

In the following sections we will use dynamical systems theory to explore various aspects of the ghostburster equations (Eq. (1)-(6)). An introduction to some of the concepts we will use can be found for example in Strogatz (1994). An alternative explanation of the burst mechanism, given in physiological terms, was presented in Doiron et al. (2001b).

Figure 5A gives the bifurcation diagram of h_d as computed from the ghostburster with I_S treated as the bifurcation parameter. We chose I_S since this is both an experimentally and physiologically relevant parameter to vary. Three distinct dynamical behaviours are observed. For $I_S < I_{S1}$ two fixed points exist; one stable, representing the resting state, and one unstable saddle. When $I_S = I_{S1}$ the stable and unstable fixed points coalesce in a saddle-node bifurcation of fixed points on an invariant circle, after which a stable limit cycle exists. This is characteristic of Class I spike excitability (Ermentrout, 1996), of which the canonical model is the well-studied θ neuron (Hoppensteadt and Izhikevich, 1997). For $I_{S1} < I_S < I_{S2}$ the stable limit cycle coexists with an unstable limit cycle. Both limit cycles coalesce at $I_S = I_{S2}$ in a saddle-node bifurcation of limit cycles. For $I_S > I_{S2}$ the model dynamics, lacking any stable periodic limit cycle, evolve on a chaotic attractor giving bursting solutions as shown in Figures 3 and 4 (lower panel). As I_S

increases further a period doubling cascade out of chaos is observed, and a period two solution exists for high I_S. The importance of both of the saddle-node bifurcations will be explored in later sections.

Figure 5B shows the observed spike discharge frequencies, f ($\equiv 1$/ISI), from the ghostburster as I_S is varied over the same range as in Figure 5A. The rest state, $I_S < I_{S1}$, admits no firing, indicated by setting f $= 0$. For $I_{S1} < I_S < I_{S2}$ the stable limit cycle attractor produces repetitive spike discharge giving a single nonzero f value for each value of I_S. f becomes arbitrarily small as I_S approaches I_{S1} from above due to the infinite period bifurcation at I_{S1}. However, for $I_S > I_{S2}$ the attractor produces a varied ISI pattern, as shown in Figures 3 and 4. This involves a range of observed f values for a given fixed I_S, ranging from ~ 100 Hz in the inter-burst interval to almost 700 Hz at the doublet firing. The burst regime, $I_S > I_{S2}$ does admit windows of periodic behaviour. A particularly large window of $I_S \in$ (13.13,13.73) shows a stable period six solution which undergoes a period doubling cascade into chaos as I_S is decreased. Finally, the period doubling cascade out of chaos for $I_S \gg I_{S2}$ is evident.

Figure 5C shows the most positive Lyapunov exponent, λ, of the ghostburster as a function of I_S. We see that $\lambda < 0$ for $I_S < I_{S1}$ because the only attractor is a stable fixed point. For $I_{S1} < I_S < I_{S2}$, $\lambda = 0$ because the attractor is a stable limit cycle. Of particular interest is that λ is positive for a range of I_S greater than I_{S2}, indicating that the bursting is chaotic. The windows of periodic behaviour within the chaotic bursting are indicated by λ being zero (e.g. the large window for $I_S \in$ (13.13,13.73)). For $I_S > 17.65$, $\lambda = 0$ because the ghostburster undergoes a period doubling cascade out of chaos, resulting in a stable period two solution.

Figure 6 is a two parameter bifurcation set showing curves for both the saddle-node

SNFP and SNLC partition parameter space into regions corresponding to quiescence, tonic firing,

will show how changes in p_d produce the characteristics of ELL bursting through the bifurcation

(10) $\tilde{p}_d = p_{d,\infty}(\langle V_d \rangle)$

where $p_{d,\infty}(\cdot)$ is the infinite conductance curve as in eq. (6). Figure 8 shows a sequence of $\tilde{p}_d$

values constructed by using $\langle V_d \rangle$ from the burst solution of the full dynamical system. This

sequence is plotted (solid circles) on top of the full $p_d(t)$ dynamics during the burst train. It is

evident that the time sequence of $\tilde{p}_d$ is of the same shape as the burst oscillation in $p_d(t)$. This is

evidence that the slow burst oscillation can be analyzed by considering $\langle V_d \rangle$.

We now complete the burst shell by adding to Figure 7A the nullcline for p_d (from eq. (6))

as well as $\langle V_d \rangle$ computed for the stable periodic solutions of the fast subsystem. This is shown in

Figure 9A. Note that as p_d decreases through p_{d1}, $\langle V_d \rangle$ decreases by ~10 mV. This is due to the

dendritic spike failure and subsequent long ISI occurring when $p_d < p_{d1}$, both contributing to lower

V_d on average (see Figure 7C). The p_d nullcline and $\langle V_d \rangle$ curves cross at $p_d = p_{d2} < p_{d1}$. Since we

have shown that the burst oscillation is sensitive to $\langle V_d \rangle$, the crossing corresponds to

$\left\langle dp_d \big/ dt \right\rangle$ changing from negative to positive (see Figure 9D).

A saddle-node bifurcation of fixed points occurs at $p_d = p_d^*$ for some $p_d^* > p_{d1}$ (data not

shown). This bifurcation is similar to the saddle-node bifurcation of fixed points in Figure 5A,

where I_S is the bifurcation parameter. This is expected, since p_d is the coefficient to a

hyperpolarizing ionic current (see eq. (3)), hence an increase in p_d is equivalent to a decrease in

depolarizing I_S. Because of the saddle-node bifurcation at $p_d = p_d^*$, the period of the period-one

limit cycle scales as $1 \big/ \sqrt{\left| p_d - p_d^* \right|}$ for p_d near p_d^* (Guckenheimer and Holmes, 1983).

With the burst shell now fully constructed (Figure 9A) we place the full burst dynamics (eq.

(7)-(8)) onto the shell. This is shown in Figure 9B. The directed trajectory is the full six

dimensional burst trajectory projected into the V_d - p_d subspace. As the burst evolves, $p_d(t)$

decreases from spike to spike in the burst. This causes the frequency of spike discharge to increase

due to the gradual shift away from the saddle-node bifurcation of fixed points at $p_d = p_d^*$.

However, once $p_d(t) < p_{d1}$ the spike dynamics shift from period-one spiking to period-two spiking.

This first produces a high frequency spike doublet, which is then followed by a dendritic potential

of reduced amplitude, causing $\langle V_d \rangle$ to decrease. When $p_d(t) < p_{d2}$, $\left\langle dp_d \middle/ dt \right\rangle > 0$ (see Figure 8D),

and $p_d(t)$ increases and is reinjected to a higher value. *The reinjection towards the " ghost" of the saddle-node bifurcation of fixed points causes the ISI (the inter-burst interval) to be long, since the*

The ghostburster system exhibits bursting, for some range of I_S, only for $2 < \tau_p < 110$ ms, with all other parameters as given in Table 1. The lower bound of τ_p is due to the fact that the inactivation of $I_{Dr,d}$ must be cumulative in order for there to be a reduction of the ISIs as the burst evolves. This requires a τ_p larger than that of the ionic channels responsible for spike production (< 1 ms). The upper bound on τ_p is also expected since significant removal of p_d inactivation during the inter-burst interval is necessary for another burst to occur. Too large a value of τ_p will not allow sufficient recovery of $I_{Dr,d}$ from inactivation and therefore bursting will not occur.

3.4- The Inter-burst Interval.

By varying I_S it is possible to set the inter-burst interval, T_{IB}, to be different lengths. This is because after the dendrite has failed (removing the DAP at the soma) the time required to produce an action potential in the somatic compartment (which is T_{IB}) is dictated almost solely by I_S. The spike excitability of the somatic compartment is Type I (Ermentrout, 1996), as evident from the saddle-node bifurcation of fixed points at $I_S = I_{S1}$. As a consequence T_{IB} is determined from the well-known scaling law associated with saddle-node bifurcations on a circle (Guckenheimer and Holmes, 1983),

$$(11) \qquad T_{IB} \sim \frac{1}{\sqrt{I_S - I_{S1}}} .$$

Figure 10 shows the average inter-burst interval, $<T_{IB}>$, as a function of $I_S - I_{S1}$ for the ghostburster with $g_{Dr,d} = 12.14$. This value of $g_{Dr,d}$ sets I_{S1} and I_{S2} close to one another (see Figure 6), allowing the system to burst with values of I_S close to I_{S1}. It is necessary to form an average due to the chaotic nature of burst solutions. Nevertheless, $<T_{IB}>$ increases as I_S approaches I_{S1}, as suggested by Eq. (11). A linear regression fit of $1/<T_B>^2$ against $I_S - I_{S1}$ gives a correlation coefficient of 0.845 further verifying that Eq (11) holds. Figure 10 also shows downward dips in $<T_{IB}>$ that occur more frequently as $I_S - I_{S1}$ goes to zero. Time series of bursts with I_S corresponding to the dips in $<T_{IB}>$ show scattered bursts with short inter-burst intervals that deviate from Eq (11), amongst bursts with longer inter-burst intervals, which fit the trend described by Eq (11). These scattered small values of T_{IB} reduce $<T_{IB}>$ for these particular values of I_S. These dips contribute to the deviation of the linear correlation coefficient cited above from 1. We do not study the dips further since the behaviour has yet to be observed experimentally. However, experimental measurements of ELL pyramidal cell burst period do indeed show a lengthening of the period as

the applied current is reduced (R.W. Turner, personal communication). This corresponds to the general trend shown in Figure 10. Eq (11) and Figure 10 show that by choosing the model parameters properly it is possible to regulate the effect of the ghost of the saddle-node bifurcation of fixed points on the burst solutions. We will show later how this property yields great diversity of time scales of possible burst solutions of the ghostburster model.

3.5⁻   *The Burst Interval – Intermittency.*

Regions of chaotic and periodic behaviour exist in many burst models (Chay and Rinzel, 1985; Terman, 1991; Terman, 1992; Hayashi and Ishizuka, 1992; Wang, 1993; Komendantov and Kononenko, 1998). The results of Figure 5 show that periodic spiking and chaotic bursting are also two distinct dynamical behaviours of the ghostburster. Moreover, the bifurcation parameter we have used to move between both dynamical regimes is the applied current I_S which mimics an average synaptic input to the cell. This indicates that changing the magnitude of input to the cell may cause a transition from periodic spiking to chaotic bursting. In ELL pyramidal cells a transition from tonic firing to highly variable bursting has been observed as applied depolarizing current is increased (Lemon and Turner, 2000; Bastian and Nguyenkim, 2001; Doiron and Turner,

sequence leaves the trapping region with a downward trend. (4) The inter-burst interval involves a sharp transition from small ISI to large ISI. (5) The ISI sequence returns to the trapping region and another burst begins.

The above description indicates that the route to chaos is Type I intermittency (Manneville and Pomeau, 1980; Guckenheimer and Holmes, 1983). Intermittency involves seemingly periodic behaviour separated by brief excursions in phase space. The clustering of points in the ISI return map in the trapping region of Figure 11A (labeled 2) is a manifestation of this apparent periodic firing. A trapping region is a characteristic feature of Type I intermittency and corresponds to a saddle-node bifurcation of limit cycles in the return map, occurring specifically at $I_S = I_{S2}$ for the ghostburster equations. The escape and return to the trapping region (regions 3,4,5 in Figure 11A) are the brief excursions. These events correspond to the period doubling transition and the cross of the

S2

4 – **Discussion**

4.1 Ghostbursting: a Novel Burst Mechanism

We have introduced a two-compartment model of bursting ELL pyramidal cells, titled the ghostburster. The model is a significant reduction of a large multi-compartmental ionic model of these cells (Doiron et al., 2001b). The large model was motivated by the 'conditional' backpropagation burst mechanism that has been experimentally characterized in ELL pyramidal cells (Lemon and Turner, 2000). The results of Lemon and Turner (2000) and Doiron et al., (2001b), suggest that the ionic requirements necessary and sufficient to support bursting as observed in the ELL are 1) action potential backpropagation along the apical dendrite sufficient to produce somatic DAPs. 2) the refractory period of dendritic action potentials must be longer than that of the somatic potentials 3) slow inactivation of a dendritic K^+ channel involved in repolarization. The fact that the ghostburster was designed to contain only these three requirements, yet succeeds in producing burst discharge comparable to experiment, suggests that these three requirements capture the essential basis of the burst mechanism used in ELL pyramidal cells.

The simplicity of the ghostburster, as compared to the large compartmental model, has allowed us to understand, from a dynamical systems perspective, the mechanism involved in this type of bursting. The ghostburster was analyzed using a separation of the full dynamical system into fast and slow subspaces (Eq (7) and (8)), similar to the analysis of many other burst models (Rinzel, 1987; Rinzel and Ermentrout, 1989; Wang and Rinzel, 1995; Bertram et al., 1995; Hoppensteadt and Izhikevich, 1997; de Vries, 1998; Izhikevich, 2000; Golubitsky et al., 2001). Treating the slow dynamical variable p_d as a bifurcation parameter with respect to the fast subsystem allowed us to construct a 'burst shell' upon which the full burst dynamics evolve. The shell shows that a transition from a period-one limit cycle to a period-two limit cycle occurs in the dynamics of the fast subsystem as p_d is reduced. The period-two limit cycle causes a sharp reduction in $<V_d>$ since the second spike of the limit cycle is of reduced amplitude, due to dendritic refractoriness. The reduction in $<V_d>$ causes the $<V_d>(p_d)$ curve to cross the p_d nullcline, and p_d(t) grows during the second ISI of the period-two orbit. The growth in p_d(t) reinjects p_d(t) near a saddle-node bifurcation of fixed points occurring at high p_d. This passage near the 'ghost' of the saddle-node bifurcation causes the ISI to be long, separating the action potentials into bursts.

Recently, Izhikevich (2000) has approached the classification of bursters from a combinatorial point of view. This has been successful in producing a large number of new fast-slow bursting mechanisms. One of these burst mechanisms has been recently observed in a biophysically plausible model of bursting corticotroph cells of the pituitary (Shorten et al., 2000). In contrast, Golubitsky et al., (2001) (extending the work of Bertram et al. (1995), and de Vries (1998)) have classified bursters in terms of the unfoldings of high codimension bifurcations. Both these methods have used the implicit assumption that burst initiation and termination involve bifurcations from quiescence (or subthreshold oscillation) to limit-cycle and vice-versa. However, our burst mechanism does not appear in any of the above classifications. This is because, the trajectories in the fast subsystem of the ghostburster are always following a limit-cycle, and are never in 'true' quiescence, corresponding to a stable fixed point. The period of the limit cycle changes dynamically because the slow subsystem is oscillating, forcing the fast system to sometimes pass near the 'ghost' of an infinite period bifurcation. Furthermore, in the ghostburster, burst termination is connected with a bifurcation from a period-one to a period-two limit cycle in the fast subsystem. This is a novel concept, since burst termination in all other burst models is connected with a transition from a period-one limit cycle to a stable fixed point in the fast subsystem (Izhikevich 2000; Golubitsky et al., 2001). Thus, while classifying burst phenomena through the bifurcations from quiescence to a period-one limit cycle and vice-versa in the fast subsystem of a dynamical bursting model has had much success, our work requires an extension of the classification of bursting to include an alternative definition of 'quiescence' and a burst attractor which is composed of only period-one and period-two limit cycles with no stable fixed points.

Rinzel (1987) shows that burst mechanisms with a one-dimensional slow subsystem require bistability in the fast subsystem in order to exhibit bursting. The slow subsystem of ghostbuster equations is one dimensional, yet Figure 9 shows that the fast subsystem x is not bistable. This would seem to be a contradiction; however, recall that as τ_p approaches values that are similar to other bursting mechanisms, bursting is not observed. Thus our results do not contradict Rinzel's previous study, yet support a separate mechanism entirely. This illustrates a key distinction between the ghostburster and conventional bursting systems; the timescale of the slow variable has an upper bound in the ghostburster. The fast and slow timescales are sufficiently separate to allow us to successfully study the burst mechanism using a quasistatic approximation.

Thus ghostbursting, while distinct, does share similarities with conventional burst mechanisms. Note that mechanisms exist similar to ghostbursting, which involve a slow passage phenomena (requiring saddle-node or homoclinic bifurcations), may exist, placing the ghostburster as only one in a family of new burst mechanisms.

The ghostburster model exhibits a threshold between tonic firing and bursting behaviour. Both Terman (1991,1992) and Wang (1993) have also identified thresholds between these behaviours in the Hindmarsh-Rose model and a modified version of the Morris-Lecar equations, respectively. Both of these models exhibited a homoclinic orbit in the fast subsystem as the spiking phase of a burst terminated. As a result, the bifurcations from continuous spiking to busting in the full dynamics were complicated. Wang observed a crises bifurcation at the transition (Grebogi et al., 1983), whereas Terman showed that a series of bifurcations occurs during the transition, which could be shown to exhibit dynamics similar to the Smale horseshoe map (Guckenheimer and Holmes, 1983). The saddle-node bifurcation of limit cycles that separates the two regimes in the Ghostburster model is a great deal simpler than either of these bifurcations. However, interestingly Wang has shown that an intermittent route to chaos is also observed in the Hindmarsh-Rose model as continuous spiking transitions into bursting, much like the Ghostburster system.

The fact that the transition from tonic firing to bursting in the Ghostburster system occurs as depolarization is increased, is in contrast to both experimental and modeling results of other bursting cells (Terman 1992; Hayashi and Ishizuka, 1992; Wang 1993; Gray and McCormick, 1996; Steriade et al., 1998; Wang, 1999). However, since many experimental and modeling results, separate from ELL, show burst threshold behaviour, the concept of 'burst excitability' may have broader implications. To expand, the saddle-node bifurcation of limit cycles marking burst threshold can be compared to the saddle-node bifurcation of fixed points, which is connected to the spike excitability of Type I membranes (Ermentrout, 1996; Hoppensteadt and Izhikevich, 1997). The functional implication of a burst threshold have yet to be fully understood, however recent work suggests that it may have important implications for both the signaling of inputs (Eugia et al., 2000) and dividing cell response into stimulus estimation (tonic firing) and signal detection (bursting) (Sherman, 2001).

4.2 Predictions for bursting in the ELL

An integral part of the burst mechanism in ELL pyramidal cells is the interaction between the soma and dendrite through action potential backpropagation. One potential function of backpropagation is thought to be retrograde signaling to dendritic synapses (Häusser et al., 2000). Further, a recent experimental study has shown that the coincidence of action potential backpropagation and EPSPs produce a significant amplification in membrane potential depolarization (Stuart and Häusser, 2001). These results may have consequences for both synaptic plasticity and dendritic computation. Our results (and those of others, see Häusser et al., 2000 for a review) imply that backpropagation can also determine action potential patterning.

As mentioned above, the ghostburster exhibits a threshold separating tonic firing and bursting as depolarization is increased. Similar behaviour has been observed in both *in vitro* and *in vivo* experimental recordings of ELL pyramidal cells (Lemon and Turner, 2000; Bastian and Nguyenkim, 2001), and in our full compartmental model simulations (data not shown). A reduction of burst threshold was observed in ELL pyramidal cells when TEA (K^+ channel blocker) was focally applied to the proximal apical dendrite (Noonan et al., 2001; Rashid et al., 2001). Our work is consistent with this observation, since dendritic TEA application is equivalent to a reduction in $g_{Dr,d}$ conductance in our model. Figure 6 shows that as $g_{Dr,d}$ is reduced burst threshold is lowered.

Bursts, as opposed to individual spikes, have been suggested to be a fundamental unit of information (Lisman, 1997). In fact, Gabbiani et al., (1996) have correlated bursts from ELL pyramidal cells with features in the stimulus driving the cell. Considering these results, it is possible that the time scale of bursting, $T (= T_B + T_{IB})$, could be tuned to sensory input, hence the ability of a bursting cell to alter T may improve its coding efficiency. A natural method to alter T would be to change the time constant(s), τ, that determine the slow process of the burst mechanism (Giannakopoulous et al., 2000). Nevertheless, to achieve an order of magnitude change in T requires a potentially large change in τ. Recently, Booth and Bose (2001) have shown, in a two-compartmental model of a bursting CA3 pyramidal cell, that the precise timing of inhibitory synaptic potentials can change the burst period T. Their results have potential implications for the rate and temporal coding of hippocampal place cells. However, the ghostburster shows that both T_B and T_{IB} can be changed by an order of magnitude, but with only small changes in either depolarizing input and/or dendritic K^+-

conceivable through realistic modulations of feedforward and feedback input which occur during electro-location and electro-communication in weakly electric fish (Heiligenburg, 1991). Changes in $g_{Dr,d}$ can further occur through the phosphorylation of dendritic K^+ channels, such as *Apt*Kv3.3 which has been shown to be abundant over the whole dendritic tree of ELL pyramidal cells (Rashid et al., 2001). Hence, the ghostbursting mechanism may offer ELL pyramidal cells a viable method by which to optimize sensory coding with regulated burst output. Further studies, quantifying the information-theoretic relevance of bursting, are required to confirm these speculations.

We conclude our study with a concrete prediction. Figures 10,12, and 13 show that the full burst period T of ELL pyramidal cells can be significantly decreased as either depolarizing current (I_S) is increased or dendritic K^+ conductance ($g_{Dr,d}$) is decreased by a small amount. This prediction can be easily verified by experimentally measuring T in bursting ELL pyramidal cells for 1) step changes in I_S, and 2) before and after TEA application to the apical dendrites, which will change $g_{Dr,d}$. Modification of other ionic currents, persistent sodium and somatic K^+ in particular, may also be used to create similar bifurcation sets as in Figure 13.

5- Acknowledgements

References

Adams WB (1985) Slow depolarization and hyperpolarizing currents which mediate bursting in an *Aplysia* neurone R15. J. Physiol. (Lond.) 360:51-

Gabbiani F, and Metzner W (1999) Encoding and processing of sensory information in neuronal spike trains. J. Exp. Biol. 202: 1267-1279.

-

bianakopoulosi F,Hauptmian CE, ooCZapp AW €0)p. urs.

Traub R, Wong R, Miles R, and Michelson H (1994). A model of a CA3 hippocampal neuron incorporating voltage-clamp data on intrinsic conductances. J. Neurophysiol. 66: 635-650.

Turner RW, Maler L, Deerinck T, Levinson SR, and Ellisman M (1994) TTX-sensitive dendritic sodium channels underlie oscillatory discharge in a vertebrate sensory neuron. J. Neurosci. 14: 6453-6471.

Turner RW, Plant J, and Maler L (1996) Oscillatory and burst discharge across electrosensory topographic maps. J. Neurophysiol. 76:2364-2382.

Turner RW, and Maler L (1999) Oscillatory and burst discharge in the apteronotid electrosensory lateral line lobe. J. Exp. Biol. 202:1255-1265.

Vetter P, Roth A, and Häusser M (2001) Propagation of action potentials in dendrites depends on dendritic morphology. J. Neurophysiol. 85:926-937.

Wang X-J (1993). Genesis of bursting oscillations in the Hindmarsh-Rose model and homoclinicity to a chaotic saddle. Physica D 62:263-274.

Wang X-J, and Rinzel J (1995). Oscillatory and bursting properties of neurons. In: ed. Arbib MA. The Handbook of Brain Theory and Neural Networks. Cambridge MA: MIT Press, pp. 686-691.

Wang X-J (1999) Fast burst firing and short-term synaptic plasticity: a model of neocortical chattering neurons. Neurosci. 89:347-362.

Figure Legends

FIG 1. ELL burst discharge and dendritic backpropagation. **A**. *In vitro* recording of burst discharge from the soma of an ELL pyramidal cell with constant applied depolarizing current. Two bursts of action potentials are shown, each exhibiting a growing depolarization as the burst evolves, causing the ISI to decrease; the burst ends with a high frequency doublet ISI. The doublet triggers a sharp removal of the depolarization, uncovering a prominent AHP, labeled a burst-AHP. **B**. Active Na^+ conductances are distributed along the soma and proximal apical dendrite of ELL pyramidal cells (left). Na^+ regions are indicated with vertical bars to the left of the schematic. Note

FIG 3. Model bursting. **A**. Time series of the somatic potential V_s during burst output. **B**. Dendritic $I_{Dr,d}$ inactivation variable p_d during the same burst simulation as in A. Note the cumulative (slow) inactivation as the burst evolves and the rapid recovery from inactivation during the inter-burst period.

FIG 4. Model performance. A single burst is obtained from ELL pyramidal cell recordings (top row; data donated by R. W. Turner), full multi-compartmental model simulations (middle row; simulation presented in Doiron et al., 2001b), and reduced two-compartment model simulations (bottom row; eqs (1)-(6)). All bursts are produced by applying constant depolarization to the soma (0.3 nA top; 0.6 nA middle; $I_s = 9$, bottom). The columns show both somatic and dendritic responses for each row. The reduced model somatic spike train reproduces both the *in vitro* data and full model simulation spike trains by showing the growth of DAPs and reduction in ISI as the burst evolves. All somatic bursts are terminated with a large bAHP, which is connected to the dendritic spike failure.

FIG 5. **A**. Bifurcation diagram of the ghostburster equations (Eqs (1)-(6)) as a function of the bifurcation parameter I_S. We choose h_d as the representative dynamic variable and plot h_d on the vertical axis. For $I_S < I_{S1}$ a stable fixed point (solid line) and a saddle (dashed line) coexist. A saddle-node bifurcation of fixed points (SNFP) occurs at $I_S = I_{S1}$. For $I_{S1} < I_S < I_{S2}$ stable (filled circles) and unstable (open circles) limit cycles coexist, the maximum and minimum of which are plotted. A saddle-

burst oscillation in p_d(t) is observed. It is evident that the discrete function $\tilde{p}_d$ (solid circles) tracks the burst oscillation in p_d(t). $\tilde{p}_d$ shows a monotonic decrease throughout the burst until the inter-burst interval, at which point $\tilde{p}_d$ is reinjected to a higher value. The horizontal lines are the values p_{d1}, corresponding to the period doubling transition, and p_{d2}, corresponding to the crossing of the nullcline curve with the $<V_d>$ curve. The p_d(t) reinjection occurs after p_d(t)$<p_{d2}$ as explained in the text. $\tilde{p}_d$ has been translated downward to lie on top of the p_d(t) time series. This is required because Eq (10) uses a unweighted average of V_d, given in Eq (9). This produces a $\tilde{p}_d$ series which occurs at higher values than p_d(t) because Eq (9) and (10) ignore the low pass characteristics of Eq (6). However, only the shape of $\tilde{p}_d$ is of interest and this is not affected by the downward translation.

FIG 9. **A**. The bifurcation diagram of Figure 6*A* is re-plotted along with the p_d nullcline $p_{d,}$ ¥9） and （10） ignorF
-
V_d

FIG 13.   Burst Gallery. **A**. Reproduction of the two parameter bifurcation set shown in Figure 6. The letters *B-F* marked inside the Figure correspond to the (I_S, $g_{Dr,d}$) parameter values used to produce panels *B-F* respectively. Examples of the inter-burst period T_{IB} and burst period T_B for each burst train are indicated (except for the tonic solution shown in *B*). The exact I_S and $g_{Dr,d}$ values used to produce each spike train are as follows: **B**. I_S=6.5, $g_{Dr,d}$=14 **C**. I_S= 7.7, $g_{Dr,d}$=13; **D**. I_S=7.6, $g_{Dr,d}$=14; **E**. I_S=5.748, $g_{Dr,d}$=12.14; **F**. I_S=5.75, $g_{Dr,d}$=11. The vertical mV scale bar in *C* applies to all panels, however, each panel has its own horizontal time scale bar.

Table I

Current	g_{max}	$V_{1/2}$	K	t

Fig1

I_{app}

apical
dendrite

Dendritic
Na^+

Somatic
Na^+

soma

Fig2

Fig4

1

Dendritic

D

1

Dendritic   1

DAP
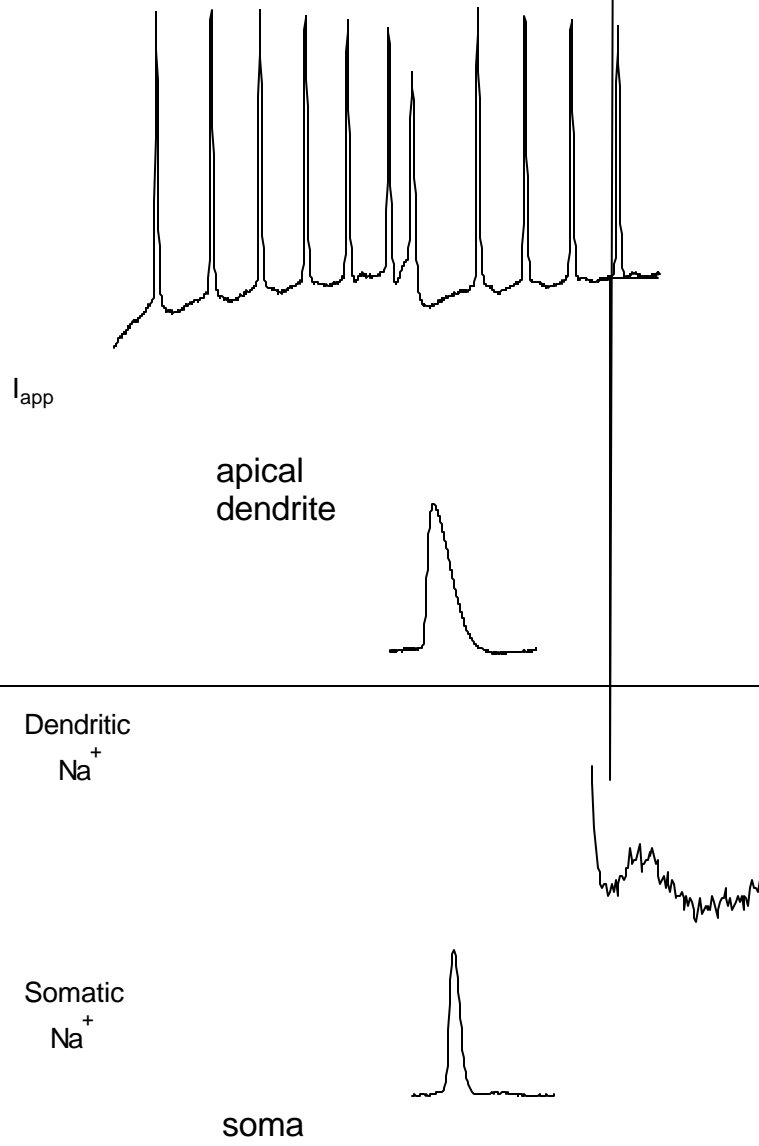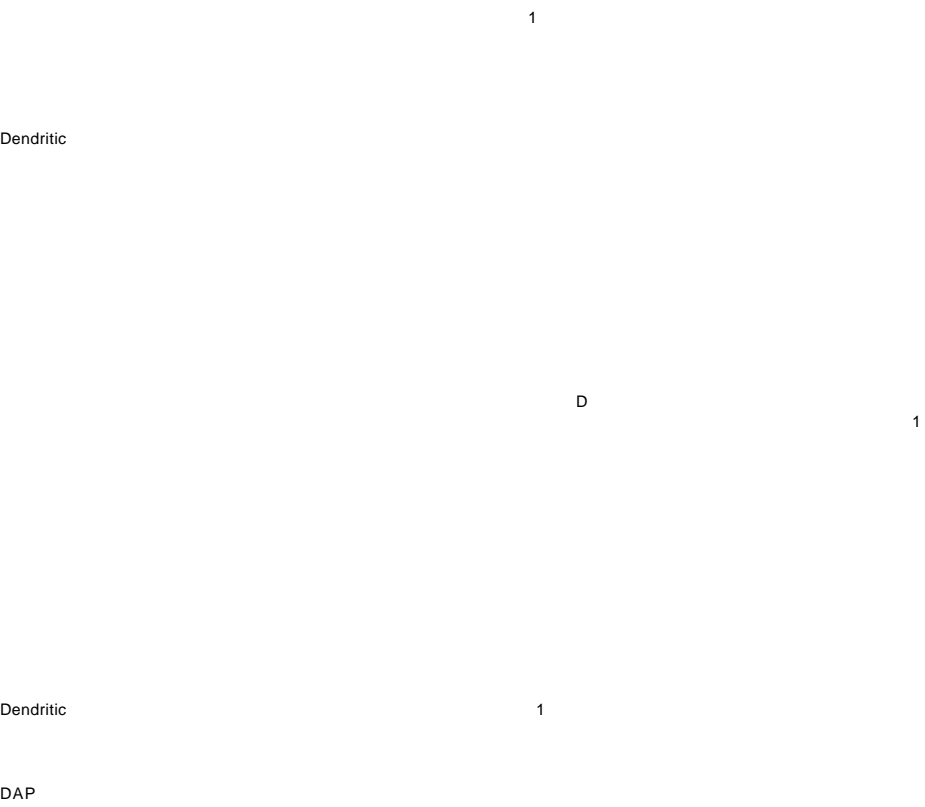
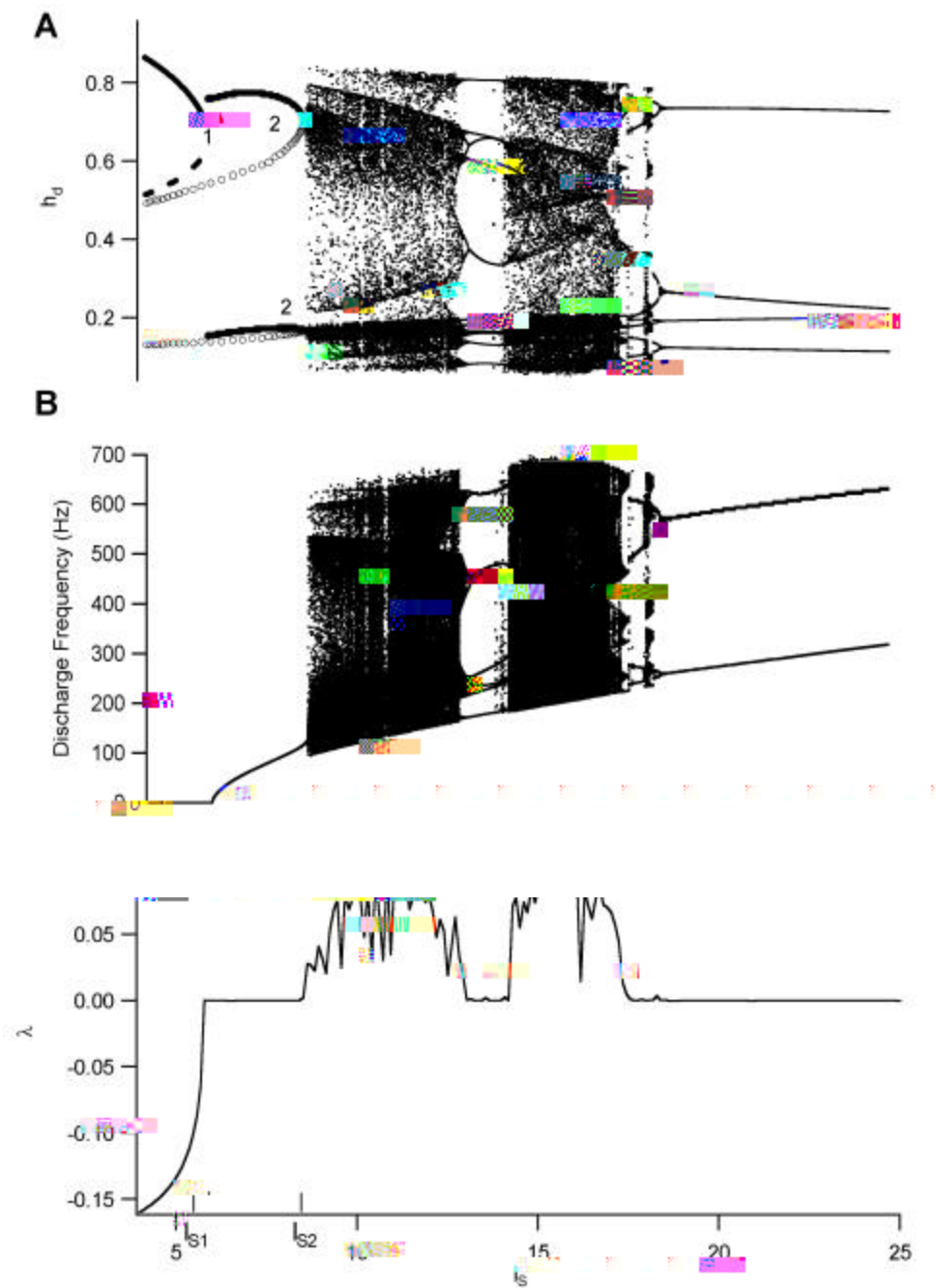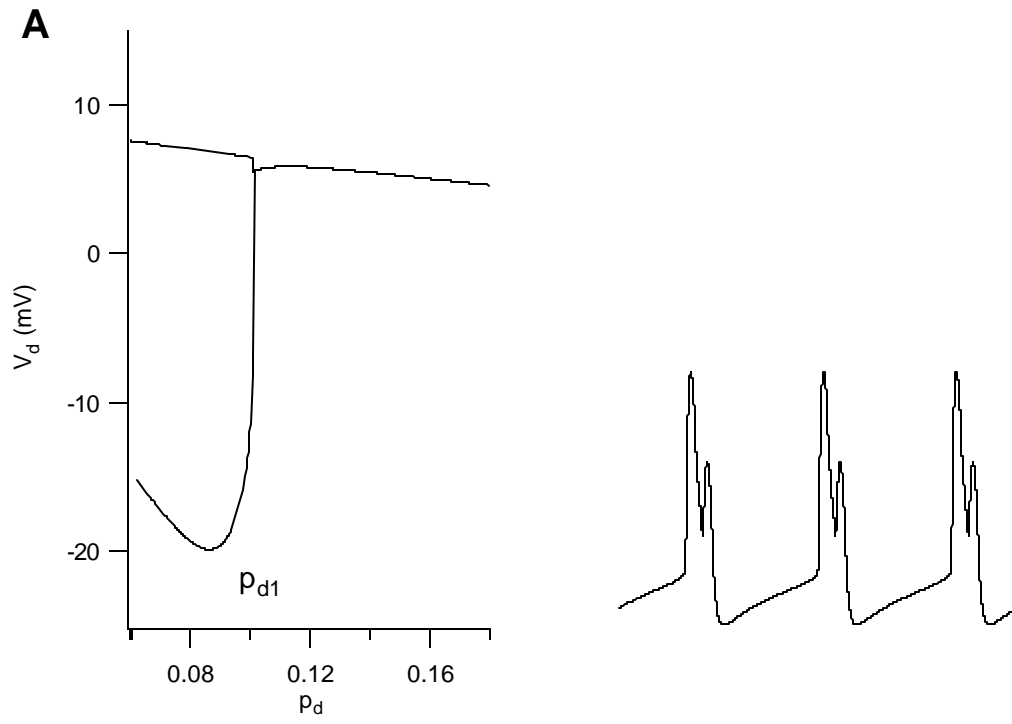**Fig5**

Fig6

Chaotic Bursting

Periodic Firing

Quiescence

Fig7

A

Fig11

Fig12

0.156c 0 Tw (0.156cTc 0300) T25 re f   BT   33